RSC Advances

PAPER

View Article Online
View Journal | View Issue

Cite this: *RSC Adv.*, 2026, **16**, 13949

3D-printed GelMA/BC@PLLAms-Cur@TCP-PCL-PEG bilayer scaffold for osteochondral repair

Enyi Gu,†[a] Kangyao Chen,†[a] Junfan Zheng,†[a] Hongxu Liu,[b] Sen Zhang,[a] Shurong Chen,*[a] Xiufeng Xiao *[c] and Tao Zhang*[a]

A functional bilayer scaffold tailored for osteochondral repair was fabricated *via* low-temperature 3D printing technology in this study. The lower layer of the scaffold was Cur@TCP-PCL-PEG, which was designed to provide robust mechanical support, realize sustained curcumin release, and thereby exert anti-inflammatory and osteogenic bioactivities. The upper layer was GelMA/BC@PLLAms, in which collagen-loaded microspheres were incorporated to effectively facilitate chondrogenic differentiation of stem cells. Comprehensive characterization revealed that the prepared bilayer scaffold possessed excellent printability, a distinct and well-integrated layered structure, and compressive strength matching the physiological requirements of osteochondral tissue. *In vitro* drug release assays confirmed the sustained release profile of curcumin from the scaffold, which conferred remarkable *in vitro* anti-inflammatory effects. Cytocompatibility evaluations demonstrated that the bilayer scaffold had superior biocompatibility, significantly promoting cell proliferation without inducing any cytotoxicity. Furthermore, *in vitro* differentiation experiments verified that the scaffold could efficiently induce osteogenic differentiation of pre-osteoblasts and enhance chondrogenic differentiation of chondrocytes and bone marrow mesenchymal stem cells, synergistically integrating the functional advantages of both the upper and lower layers. Collectively, this integrated 3D-printed bilayer scaffold exhibits prominent anti-inflammatory activity, favorable biocompatibility, and dual-lineage differentiation potential for osteogenesis and chondrogenesis, thus providing a novel and promising therapeutic strategy for the regenerative repair of osteochondral defects.

Received 7th October 2025
Accepted 5th March 2026

DOI: 10.1039/d5ra07655b

rsc.li/rsc-advances

1. Introduction

Osteochondral defects, often caused by trauma or osteoarthritis, present significant clinical challenges for repair due to the avascular nature and weak self-healing capacity of cartilage, coupled with the limited efficacy of traditional methods like microfracture and autologous chondrocyte transplantation.[1,2] Integrated bilayer scaffolds, which mimic the stratified structure and functional characteristics of native osteochondral tissue, offer a promising solution for the simultaneous regeneration of both cartilage and subchondral bone. The core design concept of these bilayer scaffolds involves material differentiation between the upper layer (for cartilage repair) and the lower layer (for bone repair), respectively matching the low modulus requirement of cartilage and the high mechanical strength requirement of bone.

Eckstein *et al.* designed a bilayer composite hydrogel scaffold that achieved target moduli for the cartilage and bone layers through different compositions,[3] effectively matching tissue mechanics. Furthermore, scaffolds are often incorporated with bioactive components to enhance functionality. For instance, the bone phase may incorporate ceramics such as hydroxyapatite (HA) or tricalcium phosphate (TCP) to promote osteogenesis,[4,5] while the cartilage layer may contain chondroitin sulfate, hyaluronic acid, or growth factors (*e.g.*, BMP-2, TGF-β) to promote chondrogenesis.[6] A wide range of materials is available for scaffold fabrication. Natural polymers like chitosan (CS),[1] agarose,[7] type II collagen,[8] and hyaluronic acid(HA)[9] are commonly used as base materials for the upper cartilage repair layer. Synthetic polymers (*e.g.*, polycaprolactone PCL, polylactic acid/poly(lactic-*co*-glycolic acid) PLGA, PEG), known for their excellent mechanical properties and controllable degradation, can provide structural support for the bone layer.[6] The fabrication method directly influences scaffold morphology and function. Currently, 3D printing, electrospinning, and freeze-drying (lyophilization) are commonly employed techniques. 3D printing technology enables the precise fabrication of multilayer scaffolds with complex internal channel structures based on digital models and allows for personalized

[a]*Department of Orthopedics, Fuzhou Second General Hospital, Fuzhou, China. E-mail: 19959161836@163.com; james155@foxmail.com*

[b]*Institute of Materia Medica, Fujian Academy of Medical Sciences, Fuzhou, China*

[c]*College of Chemistry and Materials Science, Fujian Normal University, Fuzhou, China. E-mail: xfxiao@fjnu.edu.cn*

† Enyi Gu, Kangyao Chen and Junfan Zheng contributed equally.

customization.[10] Numerous animal studies have validated that osteochondral scaffolds can simultaneously promote the regeneration of both cartilage and bone tissues, demonstrating good regenerative outcomes.[11]

This study utilizes polycaprolactone (PCL) as the matrix material for the lower layer, incorporating curcumin(Cur)-loaded polyethylene glycol (PEG)-modified tricalcium phosphate (TCP) to impart anti-inflammatory and osteogenic functions, as well as to improve mechanical properties. This Cur@TCP-PCL-PEG scaffold is fabricated *via* 3D printing. PEG is a key functional additive in composite scaffolds,[12] whose core role is to address the brittleness of scaffolds with high TCP ceramic content while ensuring biocompatibility. In addition, the hydrophilicity of PEG renders it prone to leaching in aqueous environments, and its leaching creates micropores in the polymer matrix of scaffolds. These micropores can facilitate cell infiltration and accelerate matrix degradation. Methacrylated gelatin (GelMA) is used as the matrix material for the upper layer, incorporating bovine bone collagen (BC)-loaded poly(L-lactic acid) microspheres (PLLAms) to promote chondrogenic differentiation. This GelMA/BC@PLLAms scaffold is fabricated *via* low-temperature 3D printing. The bilayer scaffold is formed by first printing the Cur@TCP-PCL-PEG scaffold, followed by continuous printing of the GelMA/BC@PLLAms scaffold on top.

2. Experimental methods

2.1 Preparation of GelMA/BC@PLLAms ink

First, bovine bone collagen-loaded poly(L-lactic acid) microspheres were prepared: 0.40 g of anhydrous ethanol was added to 9.60 g of deionized water, followed by the addition of 0.10 g of lecithin (1 wt%), denoted as solution A. 0.05 g of PLLA was dissolved in 4.95 g of 1,4-dioxane in a 60 °C water bath for 1 hour, followed by the addition of an aqueous ethylenediamine solution (1.2 wt%), and the reaction proceeded at 60 °C for 30 minutes, denoted as solution B. Subsequently, 0.5 mL of a 1 mg mL^{-1} aqueous solution of bovine bone collagen (Shanghai yuanye Bio-Technology Co., Ltd) was prepared, denoted as solution C. After solution B cooled to room temperature, solution C was added dropwise slowly into solution B under stirring. After mixing uniformly, the combined solution was added dropwise into solution A under rapid and thorough stirring for 10 minutes. After cooling to room temperature, the mixture was centrifuged at 10 000 rpm for 5 minutes. The supernatant was removed, and the precipitate was lyophilized in a vacuum freeze-dryer to obtain the bovine bone collagen-loaded poly(L-lactic acid) microspheres. Then, all the microspheres were added to 4 g of 20% GelMA solution, mixed uniformly to obtain the ink for 3D printing the upper scaffold, labeled as GelMA/BC@PLLAms.

2.2 Preparation of Cur@TCP-PCL-PEG ink

First, curcumin-loaded tricalcium phosphate was prepared: 500 mg of TCP was suspended in 10 mL of a 1.5 mg mL^{-1} curcumin solution and loaded on a shaker at 25 °C for 72 hours. The mixture was then centrifuged at 10 000 rpm for 5 minutes, and the supernatant was collected. The absorbance was measured at the maximum wavelength of 420 nm. The drug loading capacity of TCP was determined based on the standard curve of curcumin concentration *versus* absorbance. The powder obtained after centrifugation was dried in a vacuum oven to constant weight to obtain curcumin-loaded TCP.

Subsequently, 0.7060 g of PCL was completely dissolved in 1.58 mL of 1,4-dioxane in a 25 mL beaker. Then, 1 g of polyethylene glycol 400 (PEG 400) was added and mixed uniformly. Finally, 7 g of the curcumin-loaded TCP powder was added to obtain the ink for 3D printing the lower scaffold, labeled as Cur@TCP-PCL-PEG. The printing ink without curcumin loading was labeled as TCP-PCL-PEG.

2.3 3D printing fabrication of scaffolds

Using a Cellink BIO X 3D bioprinter, the Cur@TCP-PCL-PEG printing ink was loaded into a printing cartridge. A scaffold model measuring 1 cm × 1 cm × 0.5 cm with 35% infill density was selected. The printhead temperature was set to room temperature, and the printing stage temperature was set to −10 °C. The printing speed was 2 mm s^{-1}, and the pneumatic pressure for the printhead was 5 kPa. The scaffold was printed, and the completed print was placed in a freezer for cryogenic solidification to obtain the Cur@TCP-PCL-PEG scaffold. For the GelMA/BC@PLLAms scaffold, the printhead temperature was set to 35 °C, and the printed structure was crosslinked under UV light for 10 minutes for photo-curing, followed by lyophilization in a vacuum freeze-dryer to obtain the GelMA/BC@PLLAms scaffold. For the bilayer scaffold, printing started with the Cur@TCP-PCL-PEG ink. When the printing reached 50% completion, the cartridge was switched to the GelMA/BC@PLLAms printing ink to complete the remaining printing program. After lyophilization, the bilayer scaffold was obtained.

2.4 *In vitro* drug release behavior

Drug-loaded scaffold samples were individually immersed in 10 mL of phosphate-buffered saline (PBS) with a pH of 7.41, and then placed in a constant temperature shaking water bath at 37 °C with an oscillation speed of 100 rpm to simulate the normal physiological environment of tissues *in vivo*. At fixed time points, 500 μL of the release medium was withdrawn from the release system, and an equal volume of fresh PBS was immediately added to the system to maintain volume consistency. The optical density (OD) values of drug release at each time point were measured using a microplate reader. The drug concentration released from the scaffolds was determined by substituting the OD values into the standard absorbance–concentration curve established with standard drug solutions in PBS, thereby characterizing the *in vitro* drug release behavior of the drug-loaded scaffolds. All scaffold groups were tested in triplicate, and the average values were calculated.

2.4.1 Determination of bovine bone collagen content. Collagen content was determined indirectly by measuring the hydroxyproline (Hyp) content released from acid-hydrolyzed samples. After oxidation and color development reactions, the

absorbance of the resulting solution was measured using spectrophotometry. The collagen content was then calculated by multiplying the detected Hyp content by a conversion factor of 7.46. The determination of hydroxyproline (Hyp) content was performed with reference to the method described by Palka *et al.*[13]

2.5 *In Vitro* anti-inflammatory activity

The *in vitro* anti-inflammatory activity was investigated using the inhibition of albumin denaturation method. A 1% aqueous solution of bovine serum albumin (BSA) was adjusted to pH 6.5 using glacial acetic acid. A 100 mg sample of the drug-loaded scaffold was suspended in 10 mL of PBS and incubated at 37 °C. The supernatant was collected at 24 and 48 hours. 1 mL of the scaffold supernatant was added to 1 mL of the BSA solution. The solution was then heated at 70 °C for 20 min, cooled to room temperature, and the turbidity was measured at 660 nm using a microplate reader. Each scaffold group was measured in triplicate, and the average value was taken. PBS solution (without scaffold) was used as the control group. The percentage inhibition of protein denaturation was calculated using the following formula:

Inhibition percentage = (Ac − As)/Ac × 100%, where Ac is the absorbance of BSA, and As is the absorbance of BSA with the scaffold sample.

2.6 *In vitro* cell biocompatibility assessment

2.6.1 Cell culture. Mouse pre-osteoblast MC3T3-E1 cells (Beijing DingGuo ChangSheng Biotechnology Co., Ltd) were used for the experiments. MC3T3-E1 cells were cultured in 10 mL of basal medium (DMEM) containing 10% fetal bovine serum and 1% penicillin–streptomycin solution, and incubated at 37 °C in a 5% CO_2 incubator. The cell growth medium was changed every 3 days.

2.6.2 Cell proliferation. When cell density in the culture dish reached 80%, cells were digested using 0.25% trypsin/EDTA solution, collected by centrifugation, and resuspended uniformly in 1 mL of growth medium. Scaffolds (1.5 mm × 1.5 mm × 0.5 mm) were transferred to a 96-well plate and sterilized under UV light for 8 hours. Then, 100 μL of cell suspension containing 4×10^3 cells was seeded into each well. After culturing in the CO_2 incubator (5%, 37 °C) for 1, 2, 3, 4, 5, and 7 days, 10 μL of Cell Counting Kit-8 (CCK-8) solution was added to each well. After incubation under the same conditions for 2 hours, 100 μL of solution from each well was transferred to a new 96-well plate, and the optical density (OD) value was measured at 450 nm using a microplate reader. The number of proliferating cells is proportional to the OD value. Each sample was tested in triplicate, and the average value was calculated.

2.6.3 Live/dead cell staining. A live/dead cell staining kit (Calcein-AM/PI double staining kit) was used for fluorescent staining to investigate the cytocompatibility of the scaffold groups. After culturing cells for 24 and 72 hours, the medium was removed, and the cell-seeded scaffolds were gently rinsed with PBS three times. 200 μL of live/dead staining solution was added to each scaffold sample. After incubation at room temperature for 30 min, fluorescence imaging of the cells on the scaffolds was performed using an inverted fluorescence microscope. In the fluorescence images, live cells and dead cells were stained green and red, respectively.

2.7 *In vitro* osteogenic differentiation performance

2.7.1 ALP staining and ALP activity assay. To evaluate the osteogenic differentiation of MC3T3-E1 cells induced by the scaffolds, after 7 days of osteogenic induction, ALP staining was performed using a BCIP/NBT Alkaline Phosphatase Substrate Kit. Cells were fixed with 20% fixative for 30 min per well, washed thoroughly with DPBS, and then incubated with BCIP solution, NBT solution, and alkaline phosphatase chromogenic buffer at room temperature for 30 min. After staining, cells were rinsed with DPBS, and the stained mineral nodules were observed using an inverted microscope. The supernatant was collected after 7, 14, and 21 days of osteogenic induction, and the ALP concentration was detected using an alkaline phosphatase assay kit. The sample supernatant was transferred to a 96-well plate, and 50 μL of *p*-nitrophenyl phosphate substrate solution (pNPP) was added to each well. After incubation in a 5% CO_2 incubator at 37 °C for 30 min, stop solution was added to terminate the reaction. The absorbance of the samples was measured at 405 nm using a microplate reader. The alkaline phosphatase activity of the samples was calculated based on a standard curve. Three parallel experiments were conducted for statistical analysis.

2.7.2 Calcium deposition assay. Alizarin Red S (ARS) staining was used to evaluate the ability of the scaffolds to induce mineralized nodule formation. After co-culturing MC3T3-E1 cells with the scaffolds in osteogenic induction medium for 14 days, the cells were washed twice with PBS and fixed with 20% fixative for 20 min. Subsequently, the cells were stained with ARS solution for 30 min, and mineralized nodules were observed under an inverted microscope.

2.8 *In vitro* chondrogenic differentiation performance

2.8.1 Determination of glycosaminoglycan (GAG) content by dimethylmethylene blue (DMMB) colorimetric assay. 1×10^7 p3 rat chondrocytes were seeded into each well, followed by the addition of 4 mL high-glucose DMEM medium containing 20% (v/v) fetal bovine serum (FBS). The cells were cultured in a humidified incubator with 5% CO_2 at 37 °C for 7 and 14 days, respectively. Subsequently, 2 μL of prepared proteinase K solution was added to each well and incubated at 37 °C for 16 hours. 20 μL of the supernatant from each sample was transferred to a 96-well plate, and then 180 μL of prepared DMMB solution was added to each well. The mixture was pipetted up and down 4–6 times to ensure uniform mixing, followed by incubation for 5 minutes in the dark. The absorbance was measured at a wavelength of 525 nm using a microplate reader. The GAG content in each scaffold sample was calculated by substituting the detected optical density (OD) values into the standard curve equation of chondroitin sulfate.

2.8.2 Evaluation of chondrogenic differentiation potential of scaffolds using bone marrow mesenchymal stem cells

(BMSCs). Porous scaffolds from four groups were placed in a 24-well plate, with glass cell climbing slides as the control group. Passage 2 BMSCs were resuspended with 0.25% trypsin, centrifuged, and then seeded onto the surface of samples at a density of 5×10^5 cells per well. The cells were cultured in a humidified incubator with 5% CO_2 at 37 °C, and the chondrogenic differentiation medium was refreshed every 3 days. After 14 days of culture, the cells were harvested, and the expression levels of Ki-67, Col-II, Acan and Sox9 genes in the cells were detected by reverse transcription quantitative polymerase chain reaction (RT-qPCR). Five parallel samples were tested for each experimental group.

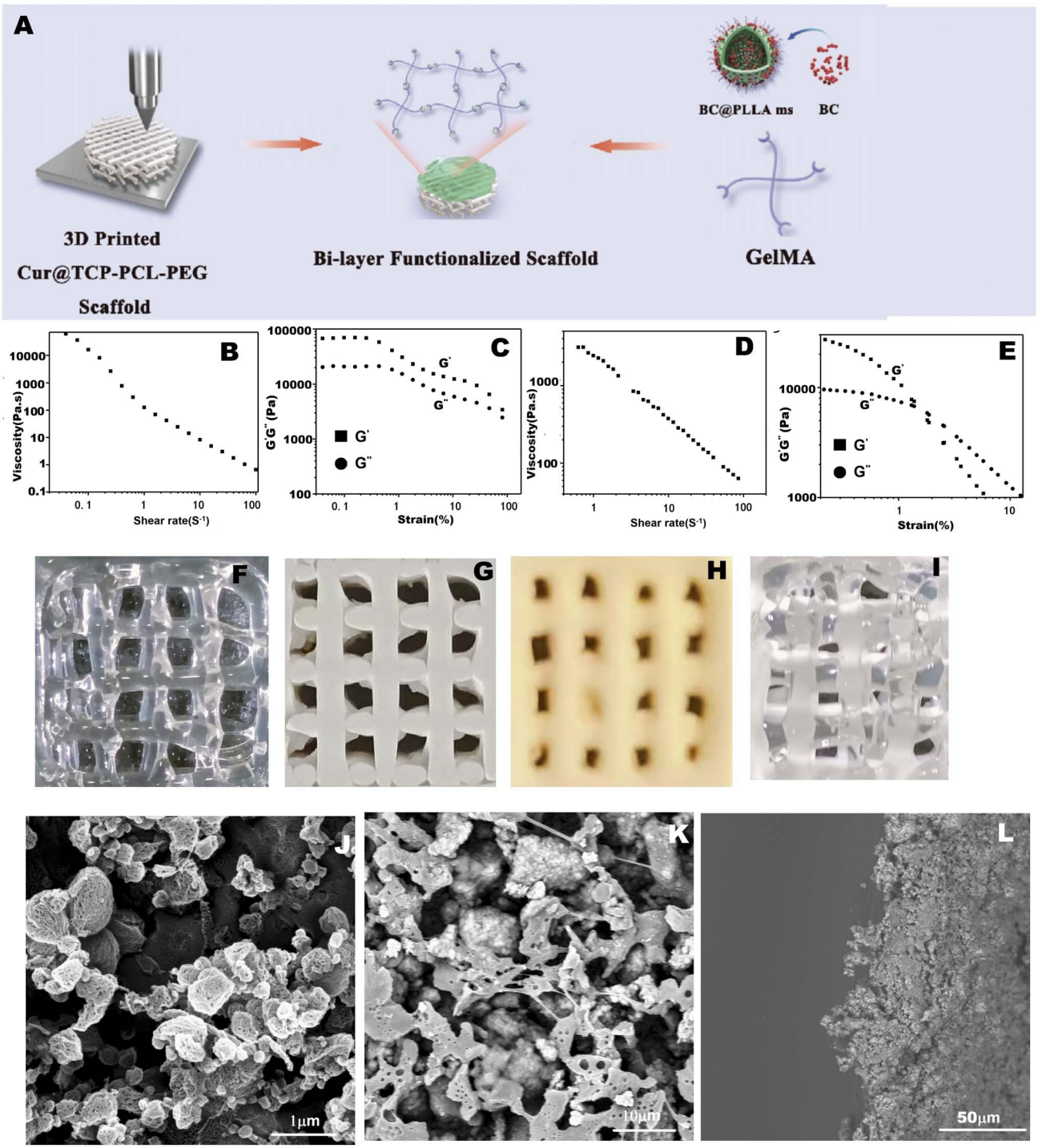

Fig. 1 (A)Schematic illustration of the fabrication process of the bi-layer scaffold; variation of viscosity with shear rate of GelMA/BC@PLLAms (B) and Cur@TCP-PCL-PEG (D); the effect of strain on storage modulus (*G′*) and loss modulus (*G″*) of GelMA/BC@PLLAms (C) and Cur@TCP-PCL-PEG (E); 3D printed scaffold physical image of GelMA/BC@PLLAms scaffold(F), TCP-PCL-PEG scaffold (G), Cur@TCP-PCL-PEG scaffold (H), bi-layer scaffold (I); SEM images of GelMA/BC@PLLAms scaffold (J), Cur@TCP-PCL-PEG scaffold (K) bi-layer scaffold (L).

2.9 Scaffold characterization

The morphology of the multifunctional scaffolds was observed using a Regulus 8100 scanning electron microscope (SEM). Simulated body fluid immersion was used to investigate the degradation behavior of the scaffolds and the *in vitro* drug release profile. The printability of the 3D printing inks was tested using a TA Discovery DHR-2 rheometer. The porosity of the scaffolds was determined by the weighing method.[14] The compressive mechanical properties of samples (6.5 × 7.5 × 5 mm) were tested using an LLOYD 5KPlus universal testing machine under ambient conditions with a 1 kN load cell. The strain was set to 80%, the load was 1 kN, and the loading rate was controlled at 0.5 mm min^{-1}. The maximum compressive strength and Young's modulus of the samples were calculated from the stress–strain curves.

2.9.1 Swelling ratio test. The initial weight of each scaffold sample was weighed and recorded as M_0. The samples were transferred to a 12-well plate, with 3 mL of PBS solution added to each well, and then incubated in a constant temperature incubator at 37 °C. At the preset time points, the samples were taken out, and the water on and around the scaffold surface was quickly blotted dry with superabsorbent filter paper. The samples were weighed again and the weight was recorded as M_1. The swelling ratio of the scaffolds was calculated using the following formula: $(M_1 - M_0)/M_0 \times 100\%$.

2.10 Statistical analysis

All data are expressed as mean ± standard deviation (SD). Results were analyzed using GraphPad Prism 9. One-way analysis of variance (ANOVA) or Tukey's test was used to determine statistical differences in the experimental data. Significance levels are denoted as $*p < 0.05$, $**p < 0.01$, $***p < 0.001$, and ns indicates no significant difference.

3. Results and discussion

3.1 Scaffold morphology

Fig. 1(A) is a schematic diagram of the 3D printed bilayer scaffold. The lower Cur@TCP-PCL-PEG scaffold was printed first. When printing reached 50% completion, the cartridge was switched to the GelMA/BC@PLLAms printing ink to complete the remaining printing program. After freeze-drying, the bilayer scaffold was obtained. Fig. 1(B) and (D) show the shear rate–viscosity curves of the GelMA/BC@PLLAms and Cur@TCP-PCL-PEG printing inks, respectively. As shown, at 25 °C, the viscosity of both printing ink materials decreased with increasing shear rate, exhibiting typical "shear-thinning" behavior.

Fig. 1(C) and (E) show the effect of strain on the storage modulus (G') and loss modulus (G'') of the GelMA/BC@PLLAms and Cur@TCP-PCL-PEG printing inks at 25 °C, respectively. As

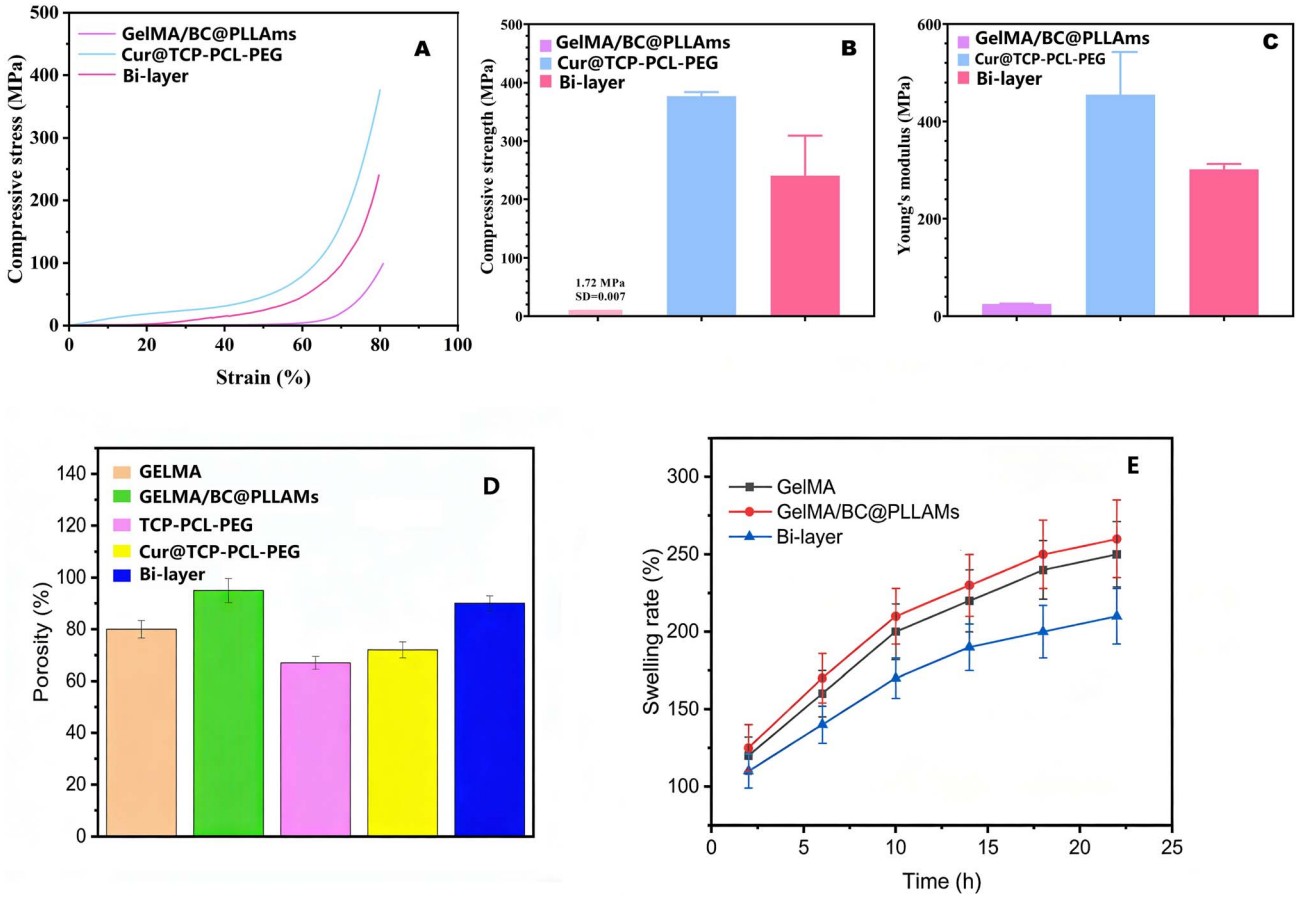

Fig. 2 (A) The mechanical properties of the scaffolds: stress–strain curves; (B) compressive strength of the scaffolds, (C) Young's modules of the scaffolds; (D) porosity of the scaffolds; (E) swelling rate of the scaffolds.

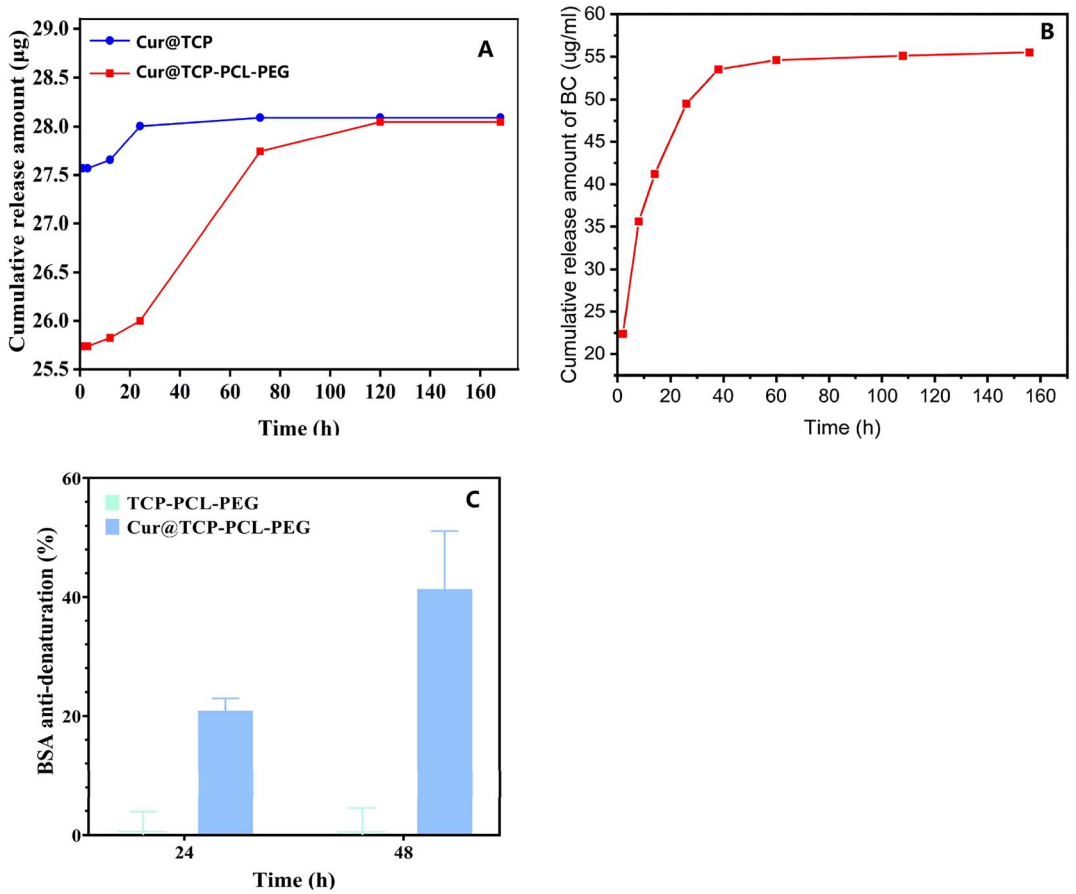

Fig. 3 (A) The cumulative release profiles of Cur from the Cur@TCP blended scaffold and Cur@TCP-PCL-PEG scaffold; (B) the cumulative release profiles of BC from bi-layer; (C) anti-BSA denaturation studies of the TCP-PCL-PEG scaffold and Cur@TCP-PCL-PEG scaffold.

shown in Fig. 1(C), the GelMA/BC@PLLAms ink experienced a brief plateau with increasing strain, after which the G' and G'' curves overall showed a decreasing trend and subsequently intersected. As shown in Fig. 1(E), the G' and G'' of the Cur@TCP-PCL-PEG ink decreased with increasing strain, followed by a rapid decline until the G' and G'' curves intersected. The results in Fig. 1(C) and (E) are consistent with the shear rate–viscosity curves shown in Fig. 1(B) and (D), respectively, demonstrating the printability of the GelMA/BC@PLLAms and Cur@TCP-PCL-PEG inks and their ability to maintain the scaffold structure after printing without significant deformation.

The macroscopic morphology of the low-temperature 3D printed scaffolds is shown in Fig. 1F–I. The GelMA/BC@PLLAms scaffold appeared transparent, the TCP-PCL-PEG scaffold was white, the curcumin-loaded Cur@TCP-PCL-PEG scaffold exhibited a yellowish-orange color, the upper and lower layers of the bilayer scaffold were aligned, and the grid structure of the scaffolds was clearly visible.

The microscopic morphology of the scaffold cross-sections is shown in Fig. 1J–L. The GelMA/BC@PLLAms scaffold contained numerous microspheres, the Cur@TCP-PCL-PEG scaffold had many granular particles, and the interface of the bilayer scaffold showed no obvious cracks, with the upper and lower layers intermingled.

3.2 Mechanical properties, porosity and swelling rate of the scaffolds

The mechanical properties of the scaffolds are shown in Fig. 2. Fig. 2(A) shows the stress–strain curves of the three scaffold samples. It can be seen that as the strain increased, the compressive strength of all three scaffolds gradually increased. The compressive strength of the Cur@TCP-PCL-PEG scaffold was significantly greater than that of the bi-layer scaffold and the GelMA/BC@PLLAms scaffold. The compressive strength of the bi-layer scaffold was intermediate between that of the GelMA/BC@PLLAms scaffold and the Cur@TCP-PCL-PEG scaffold, indicating that the bi-layer scaffold maintained relatively high compressive strength even after incorporating a high content of the inorganic component TCP. The statistical analysis results of the maximum compressive strength and modulus for the three scaffold samples are shown in Fig. 2(B) and (C), respectively. The different mechanical properties of the upper and lower layers indicate that the scaffold better meets the requirements for integrated bone-cartilage repair.

Fig. 2(D) shows the porosity of the five scaffold groups. All groups exhibited high porosity with no significant differences observed. The incorporation of BC@PLLAms slightly increased the porosity. Fig. 2(E) presents the swelling ratios of the GelMA, GelMA/BC@PLLAms, and bi-layer scaffolds. The bi-layer group

displayed the lowest swelling ratio, while the GelMA/BC@PLLAms group showed the highest. This phenomenon might be attributed to the increased porosity caused by the addition of BC@PLLAms, which facilitates water penetration and swelling.

3.3 Drug release and anti-inflammatory activity of the scaffolds

As shown in Fig. 3(A), compared to curcumin-loaded TCP powder, the release rate of curcumin from the Cur@TCP-PCL-PEG scaffold was significantly slower. After 24 hours, the release rate of curcumin from Cur@TCP-PCL-PEG accelerated noticeably, possibly due to partial degradation of the PCL matrix, exposing more curcumin-loaded TCP to the simulated body fluid. After 5 days, the release profile became essentially consistent with Cur@TCP. Fig. 3(B) shows the release profile of BC content in the bi-layer scaffold.It exhibited a relatively rapid release within the first 40 hours, and the release tended to stabilize after 40 hours.

Curcumin is a natural polyphenolic compound with strong anti-inflammatory activity. The anti-inflammatory activities of the TCP-PCL-PEG and Cur@TCP-PCL-PEG scaffolds were compared. As shown in Fig. 3(C), the inhibition rate of protein denaturation for the TCP-PCL-PEG scaffold was 0%, whereas for the Cur@TCP-PCL-PEG scaffold, the inhibition rate increased over time. At 24 hours, the inhibition rate was 20.86%, and at 48 hours, it was 41.35%, indicating that the Cur@TCP-PCL-PEG scaffold possesses good *in vitro* anti-inflammatory effects.

3.4 *In vitro* biocompatibility of scaffolds

The *in vitro* biocompatibility of the scaffolds was evaluated using the CCK-8 viability assay and live/dead fluorescence staining assay.

The results are shown in Fig. 4A. For the upper layer scaffolds, the control groups were Gelatin scaffold and GelMA scaffold, and the experimental group was GelMA/BC@PLLAms

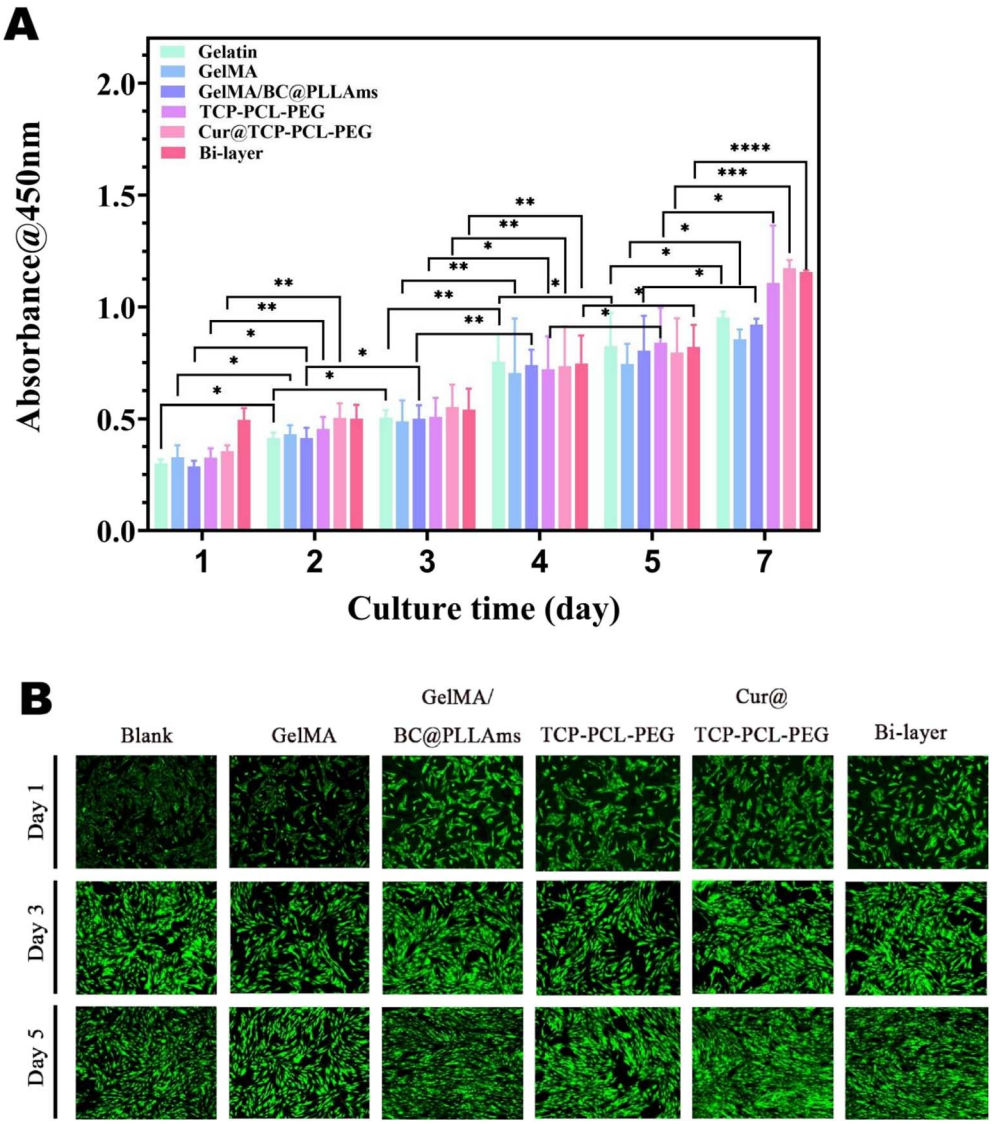

Fig. 4 The proliferation of MC3T3-E1 cells on scaffold after 1, 3, 5, and 7 days *in vitro* (A); the live(green)/dead(red) fluorescence images of MC3T3-E1 cell co-cultured with the scaffold (B).

scaffold. The OD values of the cells increased progressively, indicating cell proliferation, with significant differences observed at various time points. For the lower layer scaffolds, the control group was TCP-PCL-PEG scaffold, and the experimental group was Cur@TCP-PCL-PEG scaffold. Cells proliferated on both scaffolds, with significant differences. Compared to all control and experimental groups of the upper and lower layers, the bilayer scaffold exhibited excellent biocompatibility, with cell OD values higher than those of all other groups.

Subsequently, live/dead fluorescence staining was performed to assess cytotoxicity, as shown in Fig. 4B. No red dead cells were observed in any group, indicating that all sample groups were non-cytotoxic. For the upper layer scaffold sample groups, observation of the live/dead fluorescence images revealed that the cell density on the scaffolds loaded with bovine bone collagen was higher than that on the GelMA scaffold without bovine bone collagen, suggesting that bovine bone collagen promotes cell proliferation. For the lower layer scaffolds, the green fluorescent cell density on the Cur@TCP-PCL-PEG scaffold was higher than that on the TCP-PCL-PEG scaffold. The cell density on the bilayer scaffold was almost comparable to that on the GelMA/BC@PLLAms scaffold and the Cur@TCP-PCL-PEG scaffold.

3.5 *In vitro* osteogenic performance of scaffolds

The *in vitro* osteogenic performance of the scaffolds is shown in Fig. 5. From Fig. 5A, it can be seen that the ALP activity of

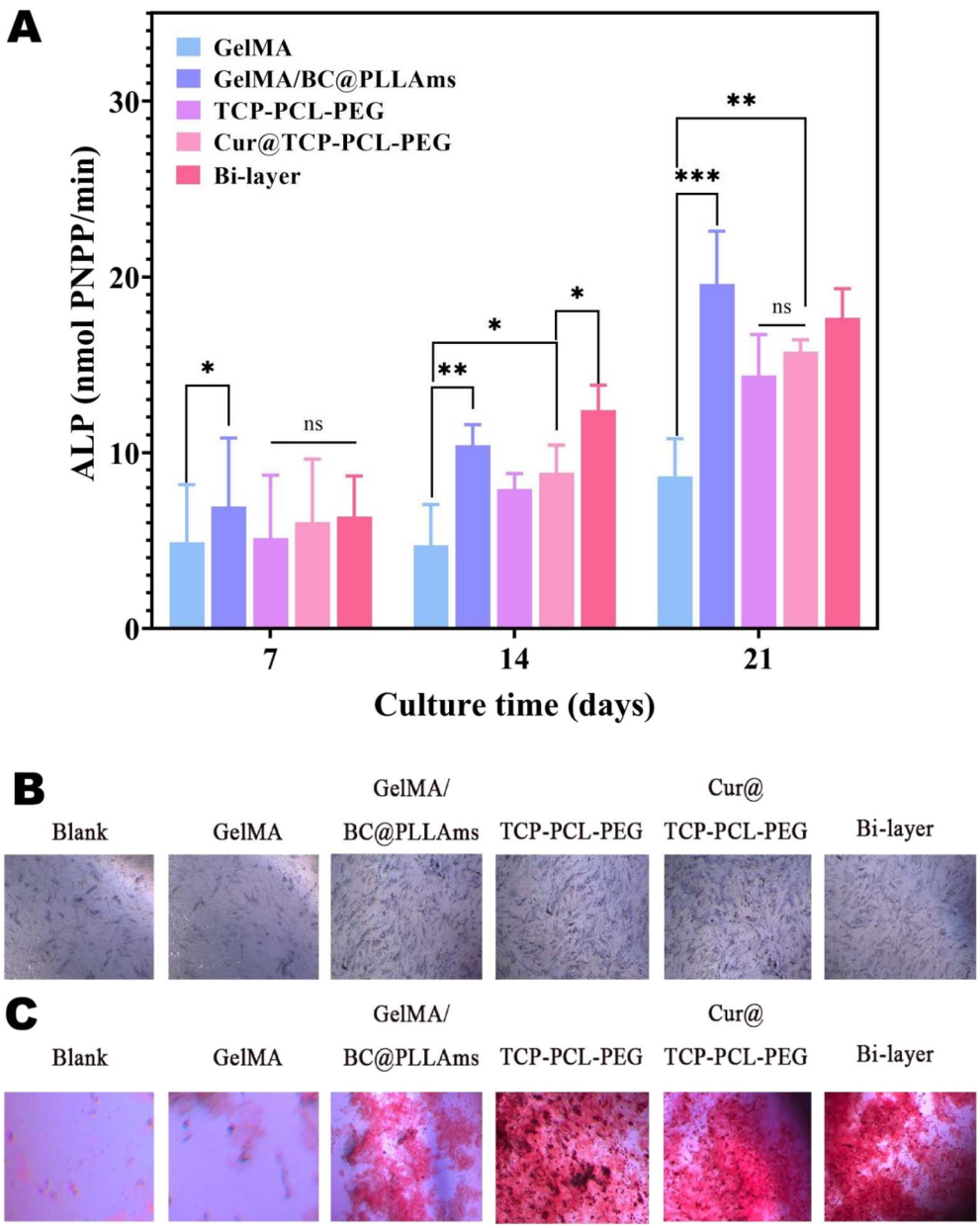

Fig. 5 The quantitative analysis of ALP activity after osteogenic induction for 7, 14 and 21 days (A); ALP staining of MC3T3-E1 cells cultured with scaffold for 14 days (B); ARS staining of MC3T3-E1 cells cultured with scaffold for 14 days (C).

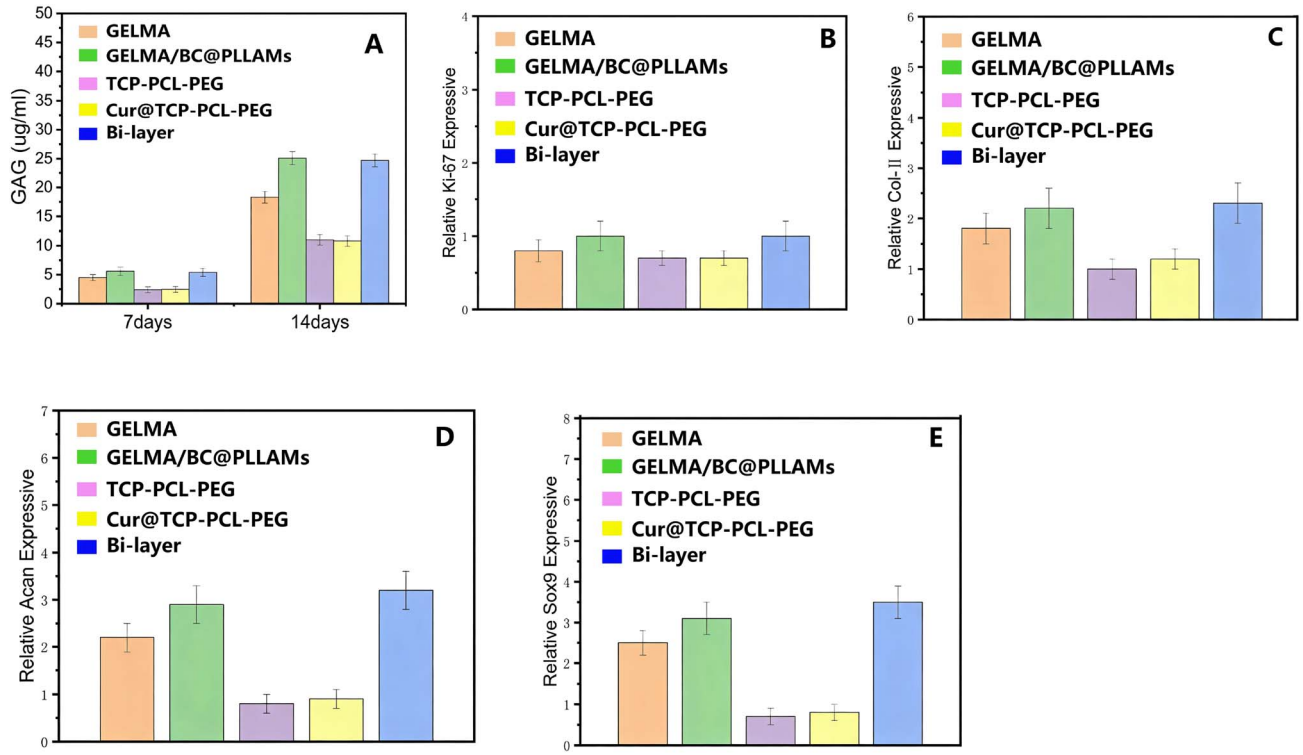

Fig. 6 (A) GAG content of the scaffolds; (B) the gene expression of Ki-67; (C) the gene expression of Col-II; (D) the gene expression of Acan; (E) the gene expression of Sox9.

the GelMA/BC@PLLAms scaffold and the bilayer scaffold was the highest compared to the other groups, indicating that bovine bone collagen has excellent osteogenic-promoting effects, beneficial for new bone formation. For the lower layer scaffolds, the osteogenic-promoting effect of TCP in the TCP-PCL-PEG and Cur@TCP-PCL-PEG scaffolds was similar, and curcumin does not possess osteogenic properties; therefore, the ALP activities of these two scaffolds were almost identical, showing no significant difference. For the bilayer scaffold, its osteogenic activity combined the effects of the upper GelMA/BC@PLLAms scaffold and the lower Cur@TCP-PCL-PEG scaffold, demonstrating its excellent ability to promote new bone formation. Fig. 5B shows the ALP staining images of the scaffolds, where areas of alkaline phosphatase activity appear blue-purple. The results are consistent with the ALP quantitative analysis.

Alizarin Red S staining is shown in Fig. 5C. For the upper layer scaffolds, it is clearly visible that the red calcium nodules in the GelMA/BC@PLLAms scaffold with added bovine bone collagen covered approximately 70% of the culture dish area, again confirming the excellent osteogenic performance of bovine bone collagen. For the lower layer scaffolds, TCP-PCL-PEG and Cur@TCP-PCL-PEG, the calcium nodules covered almost the entire culture dish for both, indicating that TCP promotes new bone formation, a result consistent with the ALP staining findings. The osteogenic effect of the bilayer scaffold was comparable to that of the TCP-PCL-PEG and Cur@TCP-PCL-PEG scaffolds, demonstrating that the modified scaffold retains good capacity for new bone formation.

3.6 *In vitro* chondrogenic performance of scaffolds

The secretion of GAG by rat chondrocytes cultured on the scaffolds was determined at 7 and 14 days. As shown in Fig. 6A, no significant difference in GAG deposition was observed among the five scaffold groups at day 7, although the GelMA/BC@PLLAms and bi-layer groups exhibited slightly higher GAG deposition than the other groups. With prolonged culture time, the GAG deposition in the GelMA/BC@PLLAms and bi-layer groups was significantly higher than that in the other groups at day 14.

The expression levels of chondrocyte proliferation-related and chondrogenic genes, including Ki-67, Col-II, Acan, and Sox9, were detected by qRT-PCR in the five scaffold groups, as shown in Fig. 6B–E. At day 1 of culture, the expression of Ki-67 showed no obvious difference among the five groups, with the GelMA/BC@PLLAms and bi-layer groups slightly higher than the others. For the Col-II gene, the highest expression was observed in the GelMA/BC@PLLAms and bi-layer groups at day 7. The expression patterns of Acan and Sox9 were similar to that of Col-II, with the most prominent expression in the GelMA/BC@PLLAms and bi-layer groups. These results demonstrate that the GelMA/BC@PLLAms and bi-layer scaffolds incorporated with BC exhibit outstanding chondrogenic performance.

4. Conclusion

In this research, a novel 3D-printed bilayer scaffold with tailored biological functions was successfully designed and fabricated for osteochondral tissue engineering applications, achieving the precise integration of structural and functional characteristics required for osteochondral repair. Through rational material selection and functional modification, the Cur@TCP-PCL-PEG lower layer not only provided the essential mechanical strength to withstand physiological mechanical stress but also realized the sustained release of curcumin for long-term anti-inflammatory effects, while the incorporated TCP endowed the layer with intrinsic osteoinductive activity to promote subchondral bone regeneration. The GelMA/BC@PLLAms upper layer constructed a biomimetic microenvironment favorable for cartilage regeneration by introducing bovine bone collagen, which effectively enhanced chondrogenic differentiation and cartilage matrix synthesis. The bilayer scaffold exhibited a stable and well-bonded layered structure with no obvious interfacial cracks, and it retained excellent biocompatibility and cytoproliferative activity. More importantly, the scaffold synergistically integrated the biological functions of the two layers, demonstrating outstanding performance in promoting both osteogenic and chondrogenic differentiation *in vitro*, which well met the dual functional demands of cartilage and subchondral bone regeneration in osteochondral defect repair. This study provides a feasible technical approach and a promising biomaterial candidate for the integrated regenerative repair of osteochondral defects, and it also lays a solid experimental foundation for the subsequent *in vivo* animal experiments and clinical translational research of 3D-printed osteochondral repair scaffolds.

Author contributions

Enyi Gu: methodology, writing-original draft preparation. Kangyao Chen: conceptualization. Junfan Zheng: data curation. Hongxu Liu: methodology. Sen Zhang: investigation. Shurong Chen: validation. Xiufeng Xiao: writing-reviewing and editing. Tao Zhang: supervision.

Conflicts of interest

The authors declare no competing financial interest.

Data availability

The data supporting this article are included within the main text. Additional data are available from the authors upon request.

Acknowledgements

This work was financially supported by Science and Technology Projects of Fujian Province (2024J011289, 2024J011300, 2022L3031, 2023D013), Fuzhou health innovation platform construction project (2021-S-wp2), Fujian Provincial Clinical Medical Research Center for First Aid and Rehabilitation in Orthopaedic Trauma (2020Y2014), Fuzhou Science and Technology Plan technology innovation platform project (2022-P-018), Fuzhou Health and Wellness Science and Technology Plan Project (2023-S-wq10).

References

1 P. Liu, M. Li, H. Yu, *et al.*, Biphasic CK2.1-coated β-glycerophosphate chitosan/LL37-modified layered double hydroxide chitosan composite scaffolds enhance coordinated hyaline cartilage and subchondral bone regeneration, *Chem. Eng. J.*, 2021, **418**, 129531.

2 J. Chen, H. Chen, P. Li, *et al.*, Simultaneous regeneration of articular cartilage and subchondral bone *in vivo* using MSCs induced by a spatially controlled gene delivery system in bilayered integrated scaffolds, *Biomaterials*, 2011, **32**(21), 4793–4805.

3 K. N. Eckstein, J. E. Hergert, A. C. Uzcategui, S. A. Schoonraad, S. J. Bryant, R. R. McLeod and V. L. Ferguson, Controlled mechanical property gradients within a digital light processing printed hydrogel-composite osteochondral scaffold, *Ann. Biomed. Eng.*, 2024, **52**(8), 2162–2177.

4 Y. Guo, X. Peng, B. Cao, *et al.*, A bilayer scaffold of collagen and nanohydroxyapatite promotes osteochondral defect repair in rabbit knee joints, *Bone & Joint Research*, 2025, **14**(2), 155–165.

5 Y. Hua, Y. Huo, B. Bai, *et al.*, Fabrication of biphasic cartilage-bone integrated scaffolds based on tissue-specific photo-crosslinkable acellular matrix hydrogels, *Mater. Today Bio*, 2022, **17**, 100489.

6 J. N. Fu, X. Wang, M. Yang, Y. R. Chen, J. Y. Zhang, R. H. Deng, Z. N. Zhang, J. K. Yu and F. Z. Yuan, Scaffold-Based Tissue Engineering Strategies for Osteochondral Repair, *Front Bioeng Biotechnol*, 2022, **9**, 812383.

7 X. Yu, Z. Deng, H. Li, *et al.*, *In situ* fabrication of an anisotropic double-layer hydrogel as a bio-scaffold for repairing articular cartilage and subchondral bone injuries, *RSC Adv.*, 2023, **13**(51), 34958–34971.

8 Z. Zhang, Y. Huang, X. Hu, *et al.*, *In situ* implantation of type II collagen-based double-layer scaffolds for articular osteochondral regeneration comprising hyaline cartilage and vascularized subchondral bones, *Bioact. Mater.*, 2025, **50**, 364–381.

9 C. Ma, T. Wang, X. Jin, *et al.*, Lineage-specific multifunctional double-layer scaffold accelerates the integrated regeneration of cartilage and subchondral bone, *Mater. Today Bio*, 2023, **23**, 100800.

10 Y. Zhai, J. Zhang, J. Li, Z. Zhao, T. Guan and D. Zhao, 3D printed osteochondral scaffolds: design strategies, present applications and future perspectives, *Front Bioeng Biotechnol*, 2024, **12**, 1339916.

11 R. Chen, J. S. Pye, J. Li, C. B. Little and J. J. Li, Multiphasic scaffolds for the repair of osteochondral defects: outcomes of preclinical studies, *Bioact. Mater.*, 2023, **27**, 505–545.

12 C. Cao, P. Huang, A. Prasopthum, A. J. Parsons, F. Ai and J. Yang, Characterisation of bone regeneration in 3D printed ductile PCL/PEG/hydroxyapatite scaffolds with high ceramic microparticle concentrations, *Biomater. Sci.*, 2021, **10**, 138–152.

13 K. Palka, Changes in intramuscular connective tissue and collagen solubility of bovine m. Semitendinosus during retorting, *Meat Sci.*, 1999, **53**(3), 189–194.

14 S. Liu, Z. He, G. Xu and X. Xiao, Fabrication of polycaprolactone nanofibrous scaffolds by facile phase separation approach, *Materials Science and Engineering: C*, 2014, **44**, 201–208.